(THIS PAGE INTENTIONALLY LEFT BLANK)

AN ABSTRACT OF THE PROJECT OF

Kory E. Kellum for the degree of Master of Science in Civil Engineering presented on May 15, 2017

Title: Seamless Topobathymetric River Mapping Through Multi-Sensor Data Integration: Lidar, Sonar, RTK GNSS and Structure from Motion

Abstract Approved:

Christopher E. Parrish

Seamless, high-resolution topobathymetric digital elevation models (DEMs) of rivers are important for generating hydrodynamic models, studying water quality and related ecological issues, modeling flood vulnerability, and numerous other applications. However, such DEMs can be difficult to generate, due to a lack of topographic and bathymetric source data. Even where the source data exist, the disparate data sets can be difficult to merge, due to differences in spatial resolutions, uncertainties, and datums. Advanced surveying technologies, including unmanned aircraft systems (UAS), structure from motion (SfM) photogrammetry, lidar, RTK GNSS, and sonar systems capable of being operated from autonomous survey boats, may assist in filling the riparian data voids, provided robust, reliable techniques can be developed for merging such data. This study investigates new methods of seamless topobathymetric river mapping using RTK GNSS, lidar, single beam echosounder and UAS-derived point clouds. As an example application, this study focuses on the evaluation of a location for a whitewater park on the Rogue River near the prior site of the Gold Ray Dam, which was removed in 2010. Data for the site were collected with a small, multirotor UAS, single beam echosounder, and GNSS. Limited existing airborne lidar data for the site were also available. A data merge approach to remotely measure river geomorphology and the surrounding topography was developed. The approach involves combining the multi-sensor data, based on both uncertainty and distance. The results indicate that the methodology may be viable for low-cost, high-resolution, and high-accuracy topobathymetric river mapping from disparate source data, supporting whitewater park site evaluation, as well as a host of other uses.

Seamless Topobathymetric River Mapping Through Multi-Sensor Data Integration: Lidar, Sonar, RTK GNSS and Structure from Motion

by
Kory E. Kellum

A PROJECT

submitted to

Oregon State University

in partial fulfillment of
the requirements for the
degree of

Master of Science

Presented May 15, 2017
Commencement June 2017

Master of Science project of Kory E. Kellum presented on May 15, 2017.

APPROVED:

Dr. Christopher Parrish representing Civil Engineering

Dean of the College of Engineering

Dean of the Graduate School

I understand that my project will become part of the permanent collection of Oregon State University Libraries. My signature below authorizes release of my project to any reader upon request.

Kory E. Kellum, Author

ACKNOWLEDGEMENTS

I would like to acknowledge and express sincere appreciation for the following people, for all of their hard work and/or assistance within the scope of this project:

- My fiancé Josephine Karz for her love and support
- Dr. Christopher Parrish for funding this research project
- Chase Simpson for providing surveying assistance during data acquisition
- Richie Slocum for helping me to improve my MATLAB skills throughout this project
- SOTAR Whitewater Manufacturing and Zet Kayaks USA for donating white water vessels
- Jackson County Parks for allowing access to the Gold Ray Dam site
- River Design Group, Inc. for providing information on the Gold Ray Dam and Ti'Lomikh Falls locations
- Mike O'Shea for lending us his outboard motor
- Leica Geosystems and David Evans & Associates for providing the surveying equipment and software
- ODOT for providing the ORGN, and
- Oregon Lidar Consortium for providing airborne Lidar data

TABLE OF CONTENTS

Page

1 Introduction 1
1.1 Example Application and Study Site 2
1.1.1 Site Characteristics 3
2 Materials and Methods 5
2.1 Data Collection 5
2.1.1 RTK Topography Data Collection 7
2.1.2 Structure from Motion (SfM) Data Collection 8
2.1.3 RTK Bathymetry Data Collection 10
2.1.4 Lidar Data Collection 10
2.2 Data Processing 11
2.2.1 GNSS Processing 11
2.2.2 Sonar Processing 15
2.2.3 SfM Processing 15
2.2.4 Lidar Processing 19
2.2.5 Accuracy Assessment 21
2.2.6 IDW (Traditional) 24
2.2.7 IDW Uncertainty Weighted Gridding Algorithm 24
3 Analysis 25
4 Discussion 27
5 Conclusions 29
References 31
APPENDIX 34

LIST OF FIGURES

Figure Page

1. Ti'Lomikh Falls location in relation to Gold Ray Dam site location (left). 4
2. View of River at a flow rate of 44cms looking upstream from river right. 6
3. View of river at a flow rate of 128 cms (4500 cfs) from river right. 6
4. Occupying vertical control station with a GNSS reciever, NZ0224, on river left above the railroad tracks. 8
5. Occupying GCP10 (black and white aerial target). 9
6. Attaching Sony a5000 camera to 3-axis aerial gimbal mounted to bottom of DJI S900. 9
7. Single-beam echosounder data acquisition for project site. 10
8. Data acquired (yellow-lidar, green-SfM, blue-Sonar GNSS, red-RTK GNSS). 11
9. Horizontal control Hubs (CP001, CP002, CP003) and Vertical Control Mark (NZ0224). 12
10. Before (top) and after (bottom) noise removal. 15
11. Camera locations and image overlap. 16
12. Ground Control Points overlaid onto noise-edited dense point cloud. 18
13. Example cross section used for vegetation removal. 19
14. RGB SfM point cloud (only extremely noisy points removed) with vegetation in tact. 19
15. Vegetation removal and “fuzzy” edge point removal where SfM failed (far right of terrain profile). . 19
16. Lidar points utilized in gridding algorithm, overlaid onto the historic Gold Ray Dam site imagery pre dam removal. 20
17. Lidar points utilized in gridding algorithm, overlaid onto 2016 Gold Ray Dam site imagery post dam removal. 20
18. Rugged terrain within AOI 22
19. Low vegetation area difficult to access by foot (e.g. top of bank). 23
20. Areas of woody debris build up 23
21. Final merged topobathymetric DEM for the AOI, shown as a hillshade in ArcGIS. 26
22. Overlapping data colored by data source (green-SfM, red-lidar, blue-RTK topo, yellow-sonar). 27

LIST OF FIGURES (Continued)

Figure Page

23. Cross section of merged data sets colored by classification (green-SfM, red-lidar, blue-RTK topo, yellow-sonar) with axes in meters. 27
24: 15-cm vertical offset on exposed bedrock consistent throughout AOI (lower image). 28
25: Bedrock island with GCP10 located 26m away from island (closest GCP). 29

LIST OF TABLES

Table Page

1. Comparison of OPUS solution coordinate vs. ORGN coordinate for control point CP001. 12
2. Derived coordinate translation parameters for RTK GNSS Survey 1 adjusted data..... 13
3: Vertical offset between RTK adjusted data and NGS published Vertical control N70224. 13
4. Comparison of adjusted RTK coordinates and ORGN coordinates for control hubs CP002 and CP003. 14
5. Comparison of Adjusted RTK coordinates from Survey 1 to coordinates from Survey 2 for control hub CP002..... 14
6. Mean and standard deviation of the coordinates for CP003 from all three surveys. 14
7. Mean N70224 NAVD 88 orthometric height compared to NGS N70224 published height. 15
8. GCP accuracy output 17
9. Results of empirical accuracy assessment performed in LP360 21

Seamless Topobathymetric River Mapping Through Multi-Sensor Data Integration: Lidar, Sonar, RTK GNSS and Structure from Motion

1 Introduction

River engineers, planners and government officials require dense, accurate, up-to-date topographic-bathymetric data for rivers in order to produce hydrodynamic models, which are crucial for a number of applications (Hardy et al. 1999; Horritt et al. 2006; Buttner 2007; Raber et al. 2007). In order to understand hydraulic responses to whitewater features, river dynamics studies require high accuracy terrain models of both the river bed and the floodplain (Alho et al. 2009). However, seamless high-resolution topobathymetric river DEMs are rarely produced, due to the technological differences of various data acquisition methods on land and under water (Flener et al. 2013), as well as the inherent challenges in river mapping, which can include swift currents, shallow waters, dynamic flows, and seasonal variability in geomorphology.

There are a number of advanced surveying technologies that hold promise for filling topobathymetric data voids in riparian zones. Unmanned aircraft systems (UAS), combined with structure from motion (SfM) photogrammetry are currently receiving considerable attention for river mapping (Lejot et al. 2007; Javernick et al. 2014). Additionally, autonomous survey boats equipped with GNSS and sonar are also attracting attention for river channel mapping (Ferreira et al. 2009). Real-time kinematic (RTK) GNSS transects are another common means of generating river survey data (Koljonen et al. 2012; Merwade et al. 2008). A challenge, however, lies in the fact that these technologies tend to generate data with greatly differing spatial densities and uncertainties. Another common challenge is that the data may be initially referenced to different horizontal and vertical datums.

Hence, to fully leverage emerging surveying technologies and techniques for the riparian zone, new data merging techniques are of interest. This study focuses on such techniques, using, as an example application, the evaluation of a proposed whitewater park location. The study site comprises a proposed whitewater park location on the Rogue River, as well as an alternative location, approximately five miles (eight kilometers) upstream. The site was flown with a DJI S900 multirotor UAS. Additionally, RTK GNSS data were collected for a number of topographic and shallow bathymetric locations within the site. The UAS and RTK GNSS data acquisitions were planned for low-flow states. Next, sonar data were

acquired at a high-flow stage using a single-beam echosounder on a cataraft. A custom Inverse Distance Weighting (IDW) algorithm was created in Matlab in order to produce a seamless topobathymetric DEM from the input data, using both distance and uncertainty information. From the final DEM product, various hydrodynamic models can be produced for studying water quality and related ecological issues, modeling flood vulnerability, and numerous other applications. The results indicate that this combination of survey technologies may be a viable, cost-effective approach to topobathymetric river mapping, using the data merge procedures developed in this research.

1.1 Example Application and Study Site

Whitewater parks are watercourses that have been artificially modified for the purposes of creating whitewater activities for canoeists and kayakers. The presence of a whitewater park can benefit a community through river restoration and economic development (Moorman et al. 2007). Locations conducive to these parks include natural, modified, and human-made river channels (Loomis 2011). Building a whitewater park may require consent and permits from both federal and state agencies that oversee water resources, such as the Army Corps of Engineers (USACE), and the Department of Natural Resources (American Whitewater 2007). Whitewater parks are built as a recreational amenity in many rivers, and, as with the construction of other types of channel-spanning structures, they can significantly alter hydraulic conditions, affecting fish habitat. It has been noted that some of the effects can be beneficial, such as increasing pool area, which is a key component of healthy salmonid habitat and is often a primary goal of habitat-improvement projects (Larscheid and Hubert 1992; Roni et al. 2008). Deeper pools are also beneficial to fish because they provide cover and essential habitat during very low flows (Binns 1994; Harig et al. 2000). Generally, to receive a permit for a whitewater park location, an alternative study is performed on a different location, such that the impacts at the two locations can be carefully analyzed, and the better of the two options can be selected. The alternative study includes topographic and bathymetric mapping of the area in order to determine important site characteristics.

A whitewater park has been proposed on the Rogue River (Anderson 2016). The proposed location is the westernmost channel and west bank of the Rogue River at Ti'Lomikh Falls, approximately one mile (1.6 km) north of I-5 in Gold Hill, Oregon. This channel was modified as part of a historic gold mining operation, and, therefore, it is not considered to be a natural channel. A main aspect of the proposed project is the removal of the hazard of a prominent midstream boulder, known as the "Muggers Rock", which renders the channel marginally runnable for commercial whitewater rafting (Anderson 2016). Additional goals are to create a whitewater slalom rapid and several whitewater freestyle waves, and

improve the recreational value of the channel by removing the hazard. Considerations for this project include impacts on fish passage and First Nation's traditional uses. Since Coho Salmon are protected by the Endangered Species Act-subject species, fish passage impacts of the project are also an important consideration.

For purposes of demonstrating a topobathymetric data merge, this project focuses on a potential alternative location approximately five miles (8 km) upstream from Ti'Lomikh Falls, at the post-dam removal site of Gold Ray Dam. This location was home to Gold Ray Dam, one of the oldest structures on the Rogue River, until its removal in 2010. The dam sat idle for 39 years before it was removed, due to it being deemed a significant barrier to salmon and steelhead migration, as well as a liability risk for the County (HDR 2009). This location was chosen based on its significantly-altered state throughout history (natural state of the river altered numerous times since in 1904), ease of river access from both sides, ease of spectator viewing and access, minimal vegetation removal required, and scenery of the iconic Table Rock and Mt. McLaughlin. River access is available from either side, with Upper River Road located on river left and Gold Ray Estates located on river right. Additionally, this location is in close proximity to populated areas, and potential participants.

1.1.1 Site Characteristics

The geomorphology of the Gold Ray area of interest (AOI) varies throughout the reach, comprising of areas of bedrock, gravel, and sand. Immediately downstream of the dam there is a reach of exposed bedrock on river left as the Rogue River enters a canyon. Additionally, two bedrock islands lie midstream in the upper reach of the AOI with a large bedrock shelf present mid-AOI on river right, as seen in Fig. 1. Upstream of the dam was an impounded area inundated 1904-2010 with numerous sloughs and extensive riparian area. The upper section of the AOI is mostly comprised of gravel and sand, verified by vibracore samples collected by Gravity Consulting LLC (HDR 2009). A simple visual observation of the site yields existing river features present, producing natural waves and rapid formations throughout the reach. This observation displays suitable gradient for the feasibility to construct multiple standing waves or play holes.

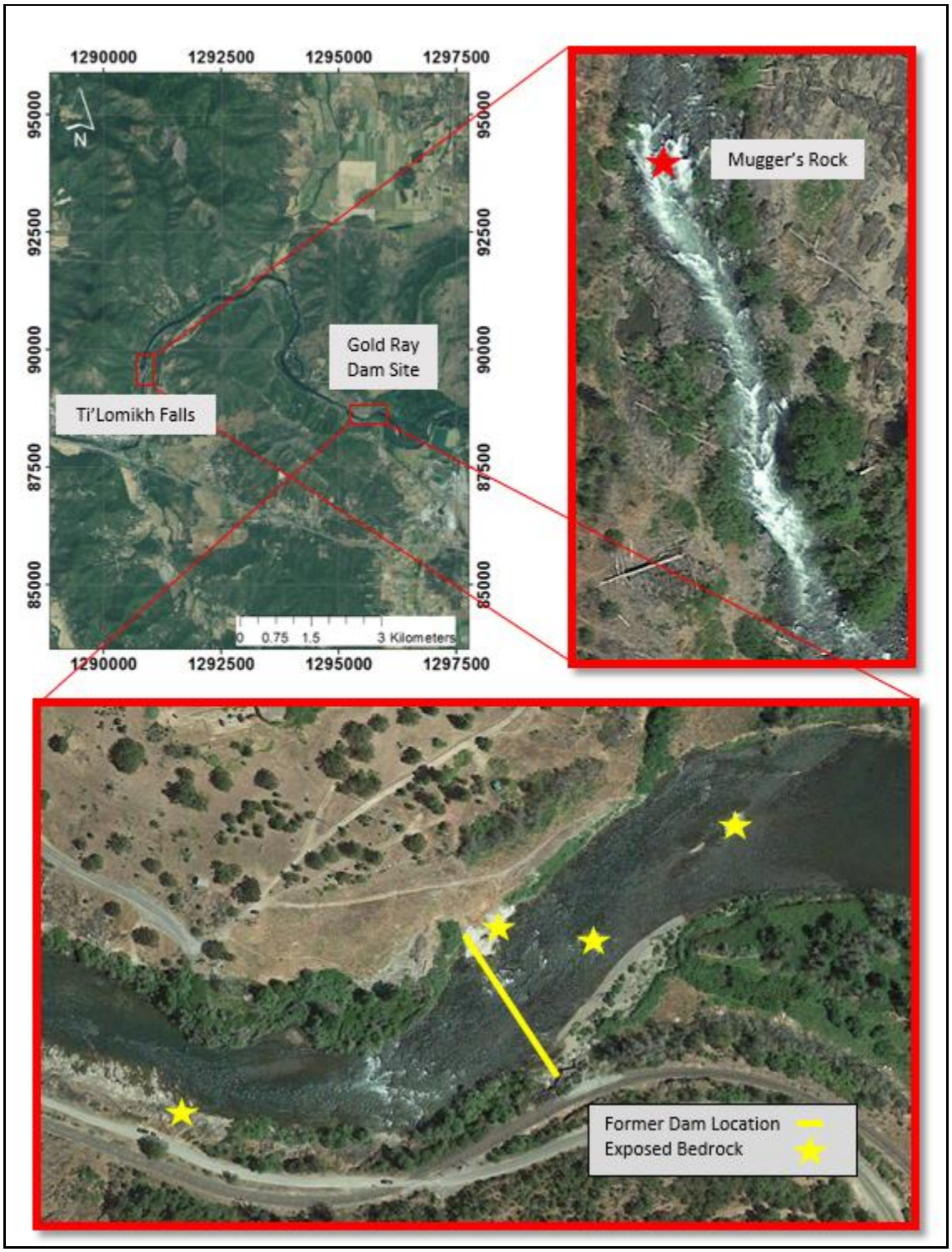

Figure 1. Ti'Lomikh Falls location in relation to Gold Ray Dam site location (left). Ti'Lomikh Falls West channel (right) with Mugger's Rock located mid-stream near the top of the channel. Gold Ray Dam Study Site (Bottom)

2 Materials and Methods

2.1 Data Collection

A common approach for generating topobathymetric river data sets is collecting RTK GNSS surveyed topographic cross-sections and integrating this data with bathymetric echosounding data (Flener et al. 2013, Maxwell and Smith 2007, Merwade et al. 2008). While small reaches of shallow rivers can be surveyed using pole-mounted RTK GNSS, the limits of these methods are reached fairly quickly with the increase in both the depth of water and the size of the area to be surveyed (Flener et al. 2013). A minimalist approach for representing fluvial terrain features while surveying topographic cross-sections is to occupy a point, on both sides of the river, at the top of the river bank (TOB) above the high water mark, a point at the edge of the water (EOW), and a point at the toe of the slope (TOS) within the water. The TOS point ensures topographic data set overlap with the bathymetric echosounding data set. Beyond collecting TOB, EOW, and TOS points, the denser the point pattern within the topographic cross sections, the more accurate the resulting DEM becomes. However, the density of the point pattern is directly proportional to the time spent surveying (Flener et al. 2013). Therefore, for longer reaches of river, incremental cross-sections are surveyed while traveling downstream, and the surveyed point pattern is generally quite sparse.

The positional accuracy of RTK-GNSS measured points can hardly be surpassed by other measuring techniques; however, remote sensing methods, such as UAS-SfM photogrammetry and echosounding techniques, can provide a much wider and denser spatial coverage (e.g., Flener et al. 2013). A common configuration for river mapping involves using a pole-mounted transducer fixed to a rigid floating watercraft. As the watercraft is propelled through the water, soundings are stored continuously in a data collector, georeferenced by a GNSS receiver affixed atop the transducer pole.

This study mapped the project site using a combination of UAS-based SfM, single-beam echosounder and RTK GNSS. Data was acquired during varying river levels:

1. Low discharge: In order to acquire SfM river data in the form of exposed bathymetry (gravel bar, sand bar, exposed bedrock, etc.) the survey team acquired SfM data on October 9th, 2016 when the river was hovering around its lowest discharge of 44 cms (cubic meters per second) or 1550 cfs (cubic feet per second). At this river stage, large gravel bars, and large areas of exposed bedrock were visible above water, as seen in Fig. 2.

Figure 2. View of river at a flow rate of 44cms, looking upstream from river right.

2. High discharge: In order to provide as much overlap as possible with the SfM data, sonar data was acquired at the highest flow feasible for data collection on December 13, 2016. This flow was estimated to be 113-142 cms (roughly 4000-5000 cfs), as shown in Fig. 3. The water level needed to be high enough to cover rocks, allowing enough depth between the outboard propeller and the river bottom, to propel the boat upstream. However, if the water level was too high, the water velocity would be too fast for the 8-hp outboard motor to propel the watercraft upstream and would not ensure multiple overlapping sonar passes.

Figure 3. View of river at a flow rate of 128 cms (4500 cfs) from river right.

Three separate surveys were performed to collect all necessary topography and bathymetry data:

- Survey 1: The first survey was performed on October 9, 2016 and included setting ground control for a UAS flight mission in order to acquire SfM data.
- Survey 2: The second survey was performed on December 12, 2016 in order to acquire Topography Data along the northern river bank, or river right.
- Survey 3: The third survey was performed the following day, December 13, 2016, to acquire bathymetry data along the river corridor, as well as finish topography data collection along the Southern river bank, or river left.

For all surveys, the RTK GNSS 3D Coordinate Quality (3DCQ) maximum limit was set to 0.05 m. Any data point failing to meet this 3DCQ threshold was not stored in the data collector.

2.1.1 RTK Topography Data Collection

RTK GNSS was used to establish temporary project control and to collect spot elevations throughout the AOI. The RTK GNSS base station was set up over a temporary control point (CP001), which consisted of a survey tack placed into a wooden survey hub driven into the ground. Two additional temporary control stations (CP002 and CP003) were also established within the site. The base station consisted of a Leica GNSS GS14 receiver attached to a 2-meter fixed height tripod. Both the base and radio/antenna setup were powered using a single deep-cycle marine battery. Two more GNSS receivers were attached to 2-meter fixed survey rods, with flat topo shoes used for the rod base, to acquire coordinates of a number of points within the Gold Ray Dam AOI. A total of 1,097 RTK points were collected within the river corridor, to be used as ground truth for the SfM point cloud, and also to fill in holes in areas where SfM failed (e.g., heavily vegetated areas).

The only National Geodetic Survey (NGS) survey mark near the Gold Ray site was a First Order Class II vertical control station, NZ0224 (Fig. 4). This mark is a standard brass disk in an area of outcropping bedrock, 0.2 km west of the intersection of the graveled road, 4.7 m south of the near rail, and 0.3 m above the tracks. The horizontal coordinates were reported by NGS to have been scaled from a topographic map. While these horizontal coordinates were not used, NZ0224 was occupied with the RTK GNSS rover as a check on the vertical accuracy of the RTK survey.

Figure 4. Occupying vertical control station with a GNSS receiver, NZ0224, on river left above the railroad tracks.

The horizontal coordinates and NAVD 88 Geoid 12B orthometric height for the base location, CP001, were established by statically occupying the hub and logging 5 hours of RINEX data. The GNSS RINEX data file collected was uploaded to NOAA's Online Positioning User Service (OPUS) to obtain coordinates for CP001, tied to the National Spatial Reference System (NSRS).

As an independent verification of the control coordinates, a 3-minute occupation on hub CP001 was performed using the GS14 GNSS receiver, receiving real-time corrections via cellular data from the Oregon Real-time GNSS Network (ORGN). ORGN occupations were performed on all three control hubs (CP001, CP002, CP003) and were compared to the other base-to-rover RTK positions.

2.1.2 Structure from Motion (SfM) Data Collection

UAS-based aerial imagery was acquired when the river was at the low discharge of 44 cms. The flights were conducted under OSU's FAA Certificate of Authorization (COA) 2016-WSA-101-COA. Before flights commenced, The RTK base, radio, and rover was configured. 12 black-and-white, "iron-cross" pattern ground, control point (GCP) photo identifiable targets were then placed throughout the scene (Fig. 5). Best efforts were made to evenly disperse the geometry of the 12 GCPs to cover the entire AOI, with GCP location placement focused on areas near the riparian zone (stream/bank interface). In addition, a few targets were placed at higher elevations throughout the site in hopes of achieving better vertical

control within the SfM point cloud. A Zet Director whitewater kayak was deployed to navigate the swift current and rapids in order to set ground control targets on islands, gravel bars, and river banks difficult to access by foot. A Leica GS14 rover was used to occupy the center of each GCP for a duration of three minutes, in order to acquire an RTK GNSS coordinate for each target location, as shown in figure 5 below.

Figure 5. Occupying GCP10 (black and white aerial target). The blue Zet Director whitewater kayak is pictured in the background.

Imagery was collected using a Sony A5000 HD digital camera affixed to a 3-axis aerial gimbal mounted to a DJI S900 hexacopter (Fig. 6). The entire setup and flights were performed between 11:30 am and 5:30 pm local on a sunny 80 °F (27 °C) day. The Mission Planner software was used to design the flight mission, collecting 340 images, with 80% overlap and 75% sidelap. The AOI flown was roughly 59,900 m^2 (48.6 acres), requiring four batteries to perform four separate 17-minute flights at a 65-m flying height above ground level (AGL) above the starting location (near CP001).

Figure 6. Attaching Sony a5000 camera to 3-axis aerial gimbal mounted to bottom of DJI S900.

2.1.3 RTK Bathymetry Data Collection

Bathymetric data was collected on December 13, 2016 between 9:00am and 3:30pm. The discharge of the Rogue River below Gold Ray Dam was 4500 cfs dropping to 4200 cfs (127-119 cms) within the data collection time frame. A SOTAR cataraft with custom aluminum frame was used to navigate the swift Rogue River current. An aluminum motor mount was designed to attach to the stern of the frame, allowing the attachment of an 8 horsepower outboard motor, as shown in Fig. 7 below. The outboard motor was used to propel the whitewater craft upstream during data collection, and laterally across the current allowing the team to survey cross sections of the river.

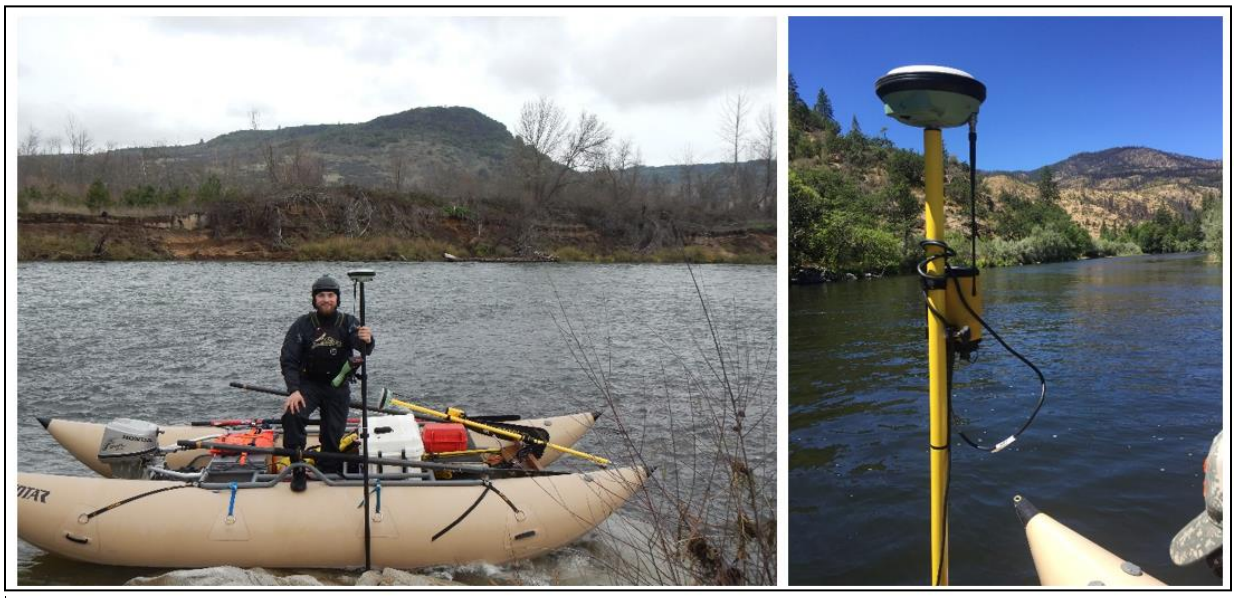

Figure 7. Single-beam echosounder data acquisition for project site.

Soundings were collected using a Seafloor Systems Inc. HydroLite-TM echosounder mounted vertically to the bow of the cataraft frame (Fig. 7), as shown in the figure above. The HydroLite transducer was attached at the bottom of a fixed survey rod, with a Leica GNSS GS14 receiver fixed at the top of the rod. The GNSS receiver was time-synced with the echosounder, allowing the user to collect both georeferenced depths and ellipsoid heights of the river bottom, stored in real-time to the Leica CS15 data collector synced to the GS14 receiver.

2.1.4 Lidar Data Collection

Watershed Sciences, Inc. collected airborne light detection and ranging (lidar) data of the Medford area for the Oregon Department of Geology and Mineral Industries (DOGAMI) in 2009. The airborne lidar dataset was downloaded from NOAA's Digital Coast data access viewer (Davidson and Miglarese 2003).

The lidar was flown on April 26, 2009. The data provider reported the absolute accuracy of the lidar data, assessed via a comparison against Real Time Kinematic (RTK) ground control points. Within the Medford Stud Area, the closest RTK points to the Gold Ray Dam AOI were collected along a 530-m section of Tolo Road, approximately 2.4 km to the southeast. The reported absolute accuracy, or deviation between laser points and RTK survey points, of the Medford area was 0.05 m (RMSE). Minimum deviations in elevation were -0.18 m and maximum deviations in elevation were 0.12m, with an average deviation of 0.04 m (Watershed Sciences 2009). Relative accuracy statistics were also reported, based on the inter-comparison of 384 flightlines and over 7 billion points. The reported relative accuracy statistics from the data provider were: mean: 0.037 m; median: 0.034 m; and standard deviation: 0.038 m.

2.2 Data Processing

Figure 8 shows the spatial extent of the acquired topographic and bathymetric data.

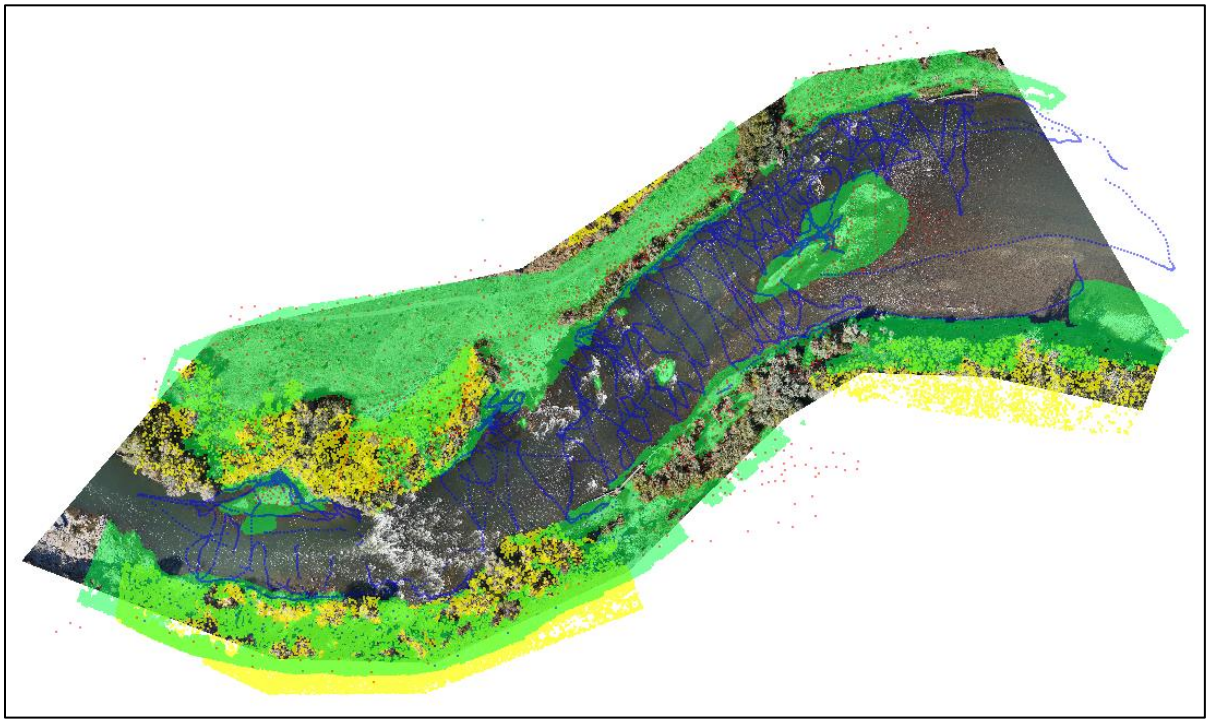

Figure 8. Data acquired (yellow-lidar, green-SfM, blue-Sonar GNSS, red-RTK GNSS).

2.2.1 GNSS Processing

The RTK base occupied a permanent hub set at CP001. Two other permanent hubs were set at locations CP002 and CP003 (Fig. 9). An NGS fist order class II vertical control hub (NZ0224) was used to constrain all surveys in the vertical direction. In order to obtain accurate coordinates for CP001, over 5

hours of static RINEX data was collected at the point, and then processed in NOAA's Online Positioning User Service (OPUS) using the precise orbits. In addition, CP001 was occupied for three minutes using a GNSS rover connected to the Oregon Real-Time Network (ORGN), to obtain additional corrected coordinates for the base location.

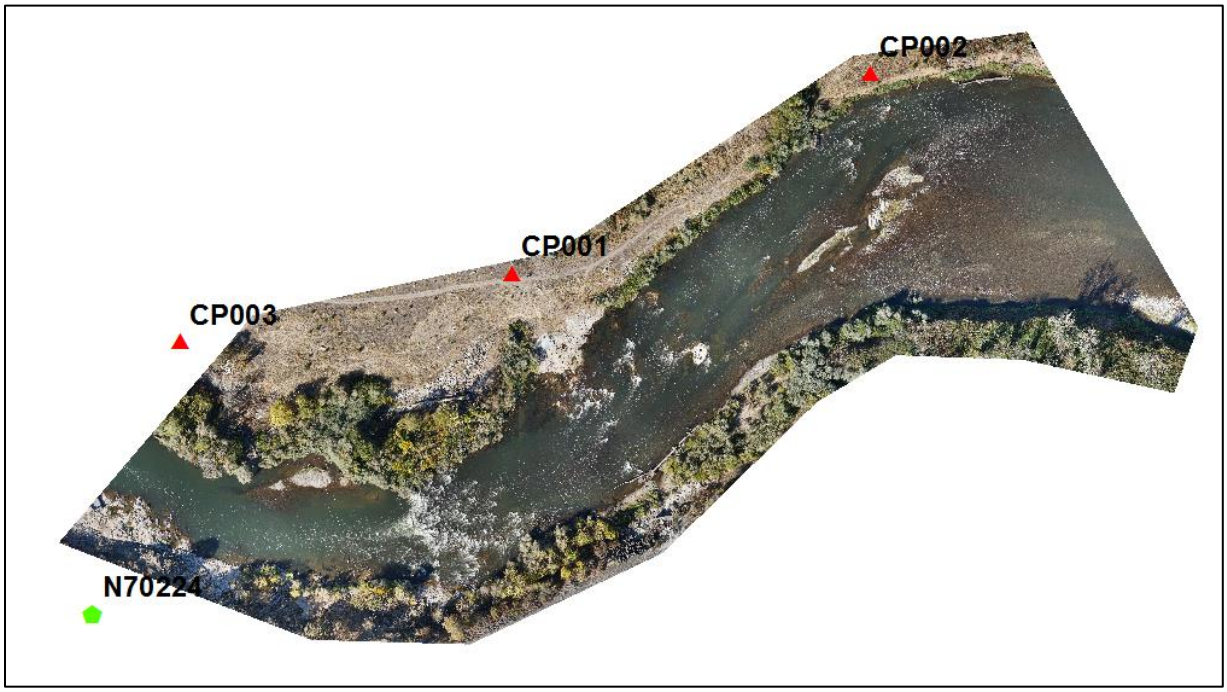

Figure 9. Horizontal control Hubs (CP001, CP002, CP003) and Vertical Control Mark (NZ0224).

When the base location is not known (and not specified during base set up), a GNSS code-based reference location, accurate within a few meters, is selected as the reference location for the base, and all real-time correction baselines are projected from the reference location. Due to all real-time correction baselines being stored in the data collector, once improved coordinates location for the base have been established, all baseline vectors can then be translated in Leica Geo Office 8.3, generating translated/adjusted coordinate values for the rest of the RTK survey data points. As a check on the base station coordinates, the OPUS solution coordinates were compared to the ORGN coordinates for CP001 (Table 1).

Table 1. Comparison of OPUS solution coordinate vs. ORGN coordinate for control point CP001.

	Northing (m)	Easting (m)	Orth. Height (m)
CP001 (OPUS)	88607.657	1295600.363	351.273
CP001 (ORGN)	88607.651	1295600.361	351.264
Difference	**0.006**	**0.002**	**0.009**

The OPUS and the ORGN coordinates agreed within millimeters in *X*, *Y*, and *Z*. The OPUS solution was chosen as the fixed coordinate for CP001, since 5 hours of occupation data was applied to that solution, as opposed to 3 minutes of occupation using the ORGN. The initial code-based estimated reference coordinates, the adjusted reference base coordinates, and the corresponding translation of all RTK values acquired during the first, October 9th, 2016, survey is shown in Table 2.

Table 2. Derived coordinate translation parameters for RTK GNSS Survey 1 adjusted data.

	Northing (m)	Easting (m)	Orth. Height (m)
Base Reference (Estimated)	88607.731	1295598.674	351.595
Base Reference (Adjusted)	88607.657	1295600.363	351.273
RTK Coordinate Translation	**-0.074**	**1.689**	**-0.322**

While performing the first RTK survey, the vertical control mark N70224 was occupied for 3 minutes. As a check on the vertical accuracy of the RTK survey, the CP001 adjusted orthometric height was compared to the published NGS orthometric height for N70224, shown in Table 3. The elevation from the rover occupation was 3.46 cm lower than the published NGS elevation. This discrepancy is not uncommon for vertical offset between RTK elevations and NGS published elevations.

Table 3: Vertical offset between RTK adjusted data and NGS published Vertical control N70224.

	Orth. Height (m)
N70224 (RTK adjusted)	356.952
N70224 (Published)	356.987
Difference	**-0.035**

While a single check point is obviously insufficient for accuracy assessment, the 3.5 cm discrepancy in the orthometric height of N70224 was taken as a rough indication of the vertical accuracy of the RTK survey for purposes of this project. Likewise, as a rough indication of the horizontal accuracy of the control survey, hubs CP002 and CP003 were occupied with the ORGN connected receiver for 3 minutes each. After the RTK baselines were adjusted, a comparison was performed on the adjusted northing, easting, and orthometric heights of the ORGN data and the adjusted RTK data (Table 4).

Table 4. Comparison of adjusted RTK coordinates and ORGN coordinates for control hubs CP002 and CP003.

	Northing (m)	Easting (m)	Orth. Height (m)
CP002 (Adjusted RTK)	88700.181	1295766.430	349.278
CP002 (ORGN)	88700.186	1295766.424	349.294
Difference	**-0.005**	**0.006**	**-0.016**
CP003 (Adjusted RTK)	88576.024	1295446.626	350.675
CP003 (ORGN)	88576.024	1295446.625	350.684
Difference	**-0.000**	**0.001**	**-0.009**

With the horizontal and vertical coordinates now established for CP001, the second and third surveys occupied the existing CP001 base location and used the known coordinates as the fixed reference base for all other baselines. Due to the base coordinates being known, no adjustments or translations were performed for surveys two and three. Because of this, CP001 for all three surveys were identical (held fixed). Table 5 shows the comparison of the coordinate CP002 from survey two with the first adjusted RTK survey coordinates. CP002 was not occupied during Survey 3.

Table 5. Comparison of Adjusted RTK coordinates from Survey 1 to coordinates from Survey 2 for control hub CP002.

Point Id	Northing (m)	Easting (m)	Orth. Height (m)
CP002 (Adjusted RTK)	88700.182	1295766.430	349.278
CP002 (Survey 2)	88700.185	1295766.428	349.272
Difference	**-0.003**	**0.002**	**0.006**

Table 6 shows the mean and standard deviation of the coordinate CP003 from all three surveys. CP003 was occupied twice during Survey 3.

Table 6. Mean and standard deviation of the coordinates for CP003 from all three surveys.

	Northing (m)	Easting (m)	Orth. Height (m)
CP003 (Adjusted RTK)	88576.024	1295446.626	350.676
CP003 (ORGN)	88576.024	1295446.625	350.685
CP003 (Survey 2)	88576.012	1295446.629	350.679
CP003 (Survey 3)	88576.016	1295446.631	350.679
CP003 (Survey 3)	88576.022	1295446.632	350.679
Mean	**88576.020**	**1295446.629**	**350.680**
Standard Deviation	**0.006**	**0.003**	**0.003**

As a rough indication of the vertical accuracy of Survey 2 and 3, the NGS mark N70224 was occupied during survey 2 for three minutes, and occupied twice on survey 3 for three minutes each. The mean

orthometric height of N70224 was calculated using the elevations established from survey 2 and 3, and was then compared to the published NGS elevation (Table 7).

Table 7. Mean N70224 NAVD 88 orthometric height compared to NGS N70224 published height

Point Id	NAVD 88 Geiod 12B Orth. Height (m)
N70224 (Survey 2)	356.968
N70224 (Survey 3)	356.97
N70224 (Survey 3)	356.97
Mean	**356.969**
N70224 (NGS published)	356.987
Difference	**-0.018**

2.2.2 Sonar Processing

Turbidity, aeration, and other in-stream factors can negatively affect sonar returns, resulting in noisy bathymetric data. It is important to extract noisy points, or outliers, from a data set in order to yield an accurate gridded dataset of the bathymetry profile. In this project, manual noise removal was performed. Fig. 10 below displays an example of bathymetry data within a cross section of the Rogue River, before and after noise extraction.

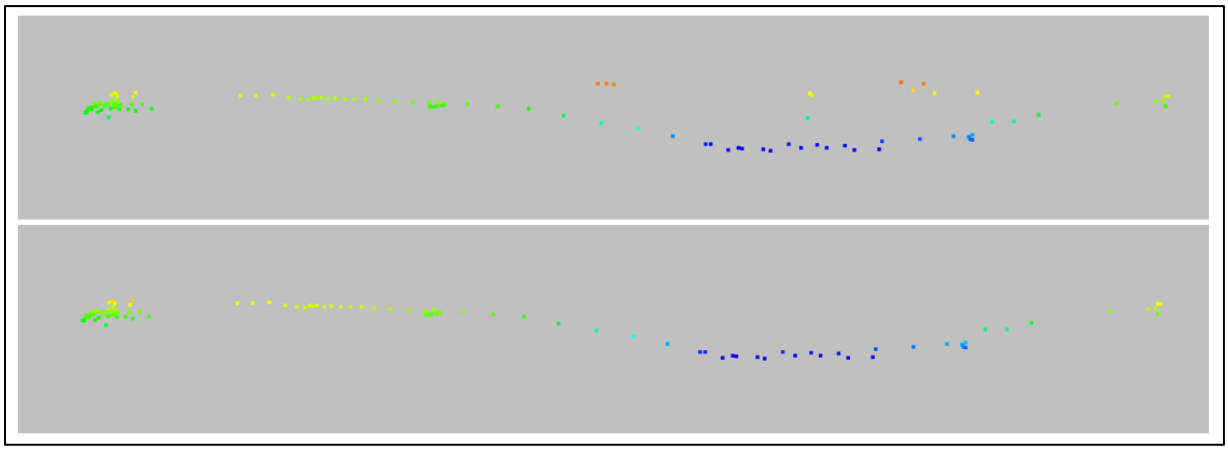

Figure 10. Before (top) and after (bottom) noise removal.

2.2.3 SfM Processing

SfM processing and point cloud generation was performed in Agisoft Photoscan version 1.2.6.2834. A total of 340 images were aligned using the highest accuracy parameter setting, with the pair preselection

parameter disabled. 40,000 key points and 5,000 tie points were set under the alignment parameters. Figure 11 shows camera locations and image overlap, with camera locations represented as black dots, and image overlap represented by the color gradient.

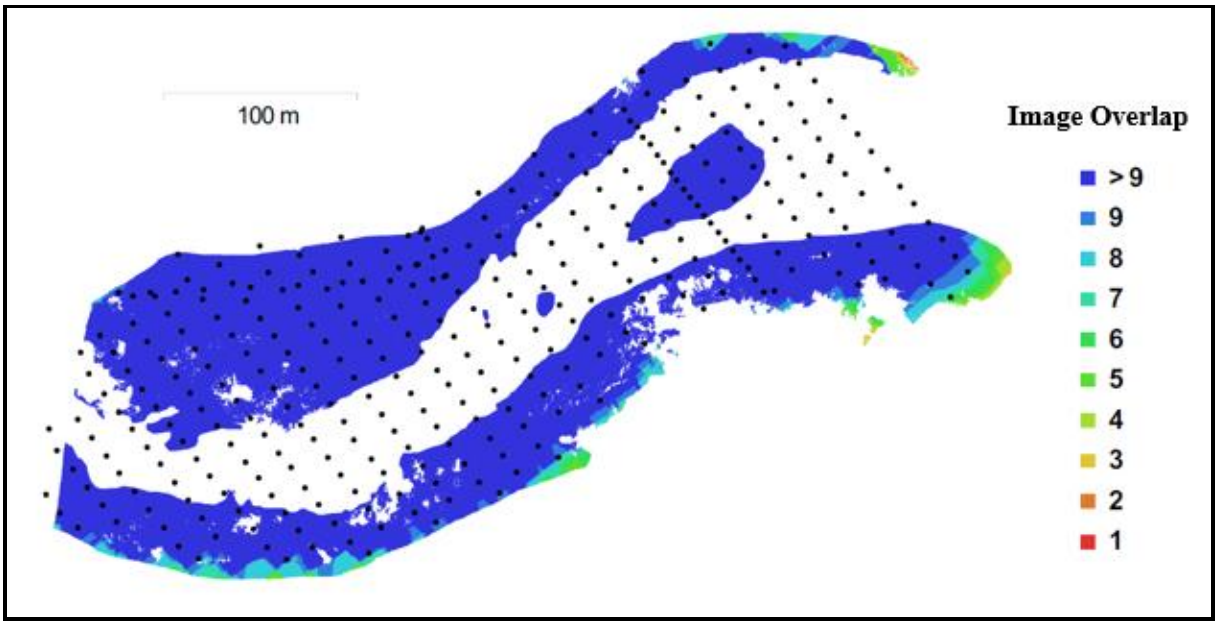

Figure 11. Camera locations and image overlap.

The Ground Control Points (GCPs) were imported as a CSV file, and the point cloud was georeferenced by matching GCP coordinates with the corresponding photo targets within the imagery. The ground sample distance (GSD) was 1.6 cm and the marker accuracy was set to 2 pixels with tie point accuracy set to 3 pixels. The sparse point cloud generated had a RMSE of 26 cm, as reported by Photoscan, with most influence coming from vertical error, due to inaccurate water and vegetation tie points. Poor water and vegetation tie points were systematically removed within the sparse point cloud. After, the cameras were realigned and the relative accuracy of the sparse point cloud was improved to 4.7 cm RMSE. Table 8 contains the control point accuracy output, as provided by Agisoft Photoscan. It is important to note however, that the reported control point accuracy statistics within the SfM software are generally overly optimistic, if taken as an indication of the overall accuracy of the point cloud (Slocum and Parrish, 2017).

Table 8. GCP accuracy output

Label	X error (cm)	Y error (cm)	Z error (cm)	3D error (cm)
GCP01	0.5	2.2	-5.0	5.5
GCP02	0.1	-0.8	5.2	5.3
GCP03	0.0	-0.1	-7.5	7.5
GCP04	-3.2	1.8	2.3	4.3
GCP05	1.1	-1.4	7.6	7.8
GCP06	-1.2	0.4	-1.1	1.7
GCP07	1.9	-1.2	2.3	3.2
GCP08	-1.3	-0.3	-5.1	5.3
GCP09	0.7	-0.4	3.7	3.8
GCP10	0.0	0.0	-4.3	4.3
GCP11	0.9	-1.1	0.5	1.5
GCP12	0.1	-0.1	0.1	0.2
RMSE	**1.3**	**1.1**	**4.4**	**4.7**

Photoscan computes the 3D error, ε_{3D}, as:

$$\varepsilon_{3D} = \sqrt{dx^2 + dy^2 + dz^2} \quad (1)$$

The RMSE is computed as:

$$\text{RMSE} = \sqrt{\frac{\sum_{i=1}^{n} v_i^2}{n}} \quad (2)$$

where n is the number of GCPs, and v_i represents an individual estimated error. The dense point cloud was then generated and false tie points were manually cleaned out of the final reconstruction within Agisoft Photoscan (Fig. 12). The dense point cloud's reconstruction parameters were high quality, and moderate depth filtering, generating nearly 56 million points.

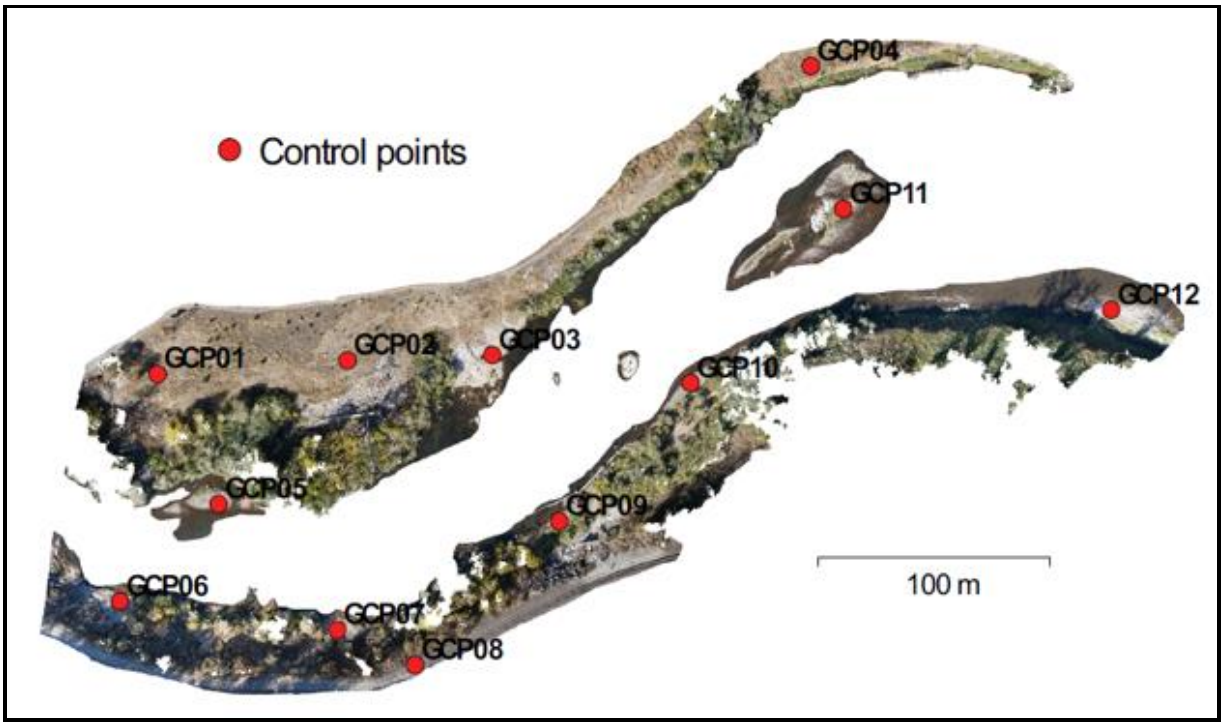

Figure 12. Ground Control Points overlaid onto noise-edited dense point cloud.

To prepare the dense point cloud for input into the IDW algorithm, removal of all vegetation and noisy points were required, in order to generate an accurate terrain model. Point reclassification (vegetation removal) was performed manually in LP360, by viewing one small profile of the terrain at a time (Fig. 13), and stepping through the data. Additionally, there were areas where SfM failed, and formed a "fuzzy" point cloud as opposed to a well-defined terrain profile, as shown on the right side of the land profile in Fig. 14 below. These "fuzzy" areas did not have high accuracy and were classified as noise (Fig. 15).

Figure 13. Example cross section used for vegetation removal.

Figure 14. RGB SfM point cloud (only extremely noisy points removed) with vegetation in tact.

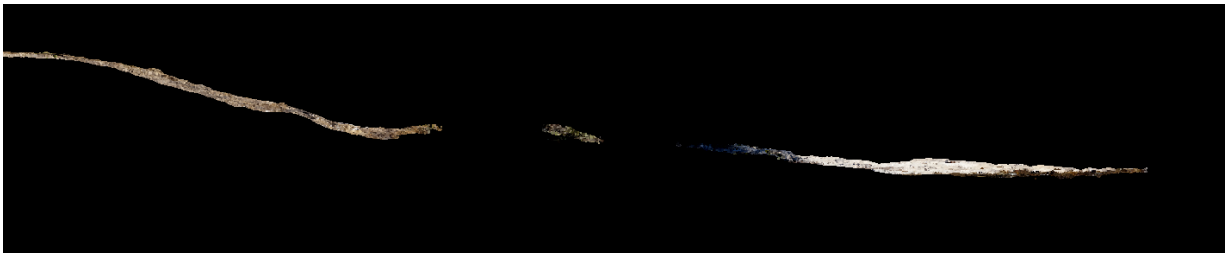

Figure 15. Vegetation removal and "fuzzy" edge point removal where SfM failed (far right of terrain profile).

2.2.4 Lidar Processing

The 2009 Medford area lidar was flown prior to dam removal in 2010, and therefore has significant temporal changes as compared to the current state of the AOI. Upstream of the dam had the most significant temporal changes. However, a few small areas within the AOI had not been affected by the

dam removal, and were used in the gridding process, primarily to fill in data voids in areas of dense vegetation. These areas were non-inundated by the dam impoundment, and thus remained unchanged by the change in water stage post dam removal. In order to detect these unaffected areas, historic aerial imagery was compared to current imagery of the AOI, in order to begin isolating areas within the lidar data that appeared visually unchanged (Fig. 16). Overlapping RTK GNSS data were then used to verify the undisturbed locations, by analyzing cross sections within LP360, and manually extracting lidar data with significant vertical differences (greater than 0.5 meters) from the reference data. Figures 16 and 17 show the lidar data that was incorporated in the gridding algorithm.

Figure 16. Lidar points utilized in gridding algorithm, overlaid onto the historic Gold Ray Dam site imagery pre dam removal.

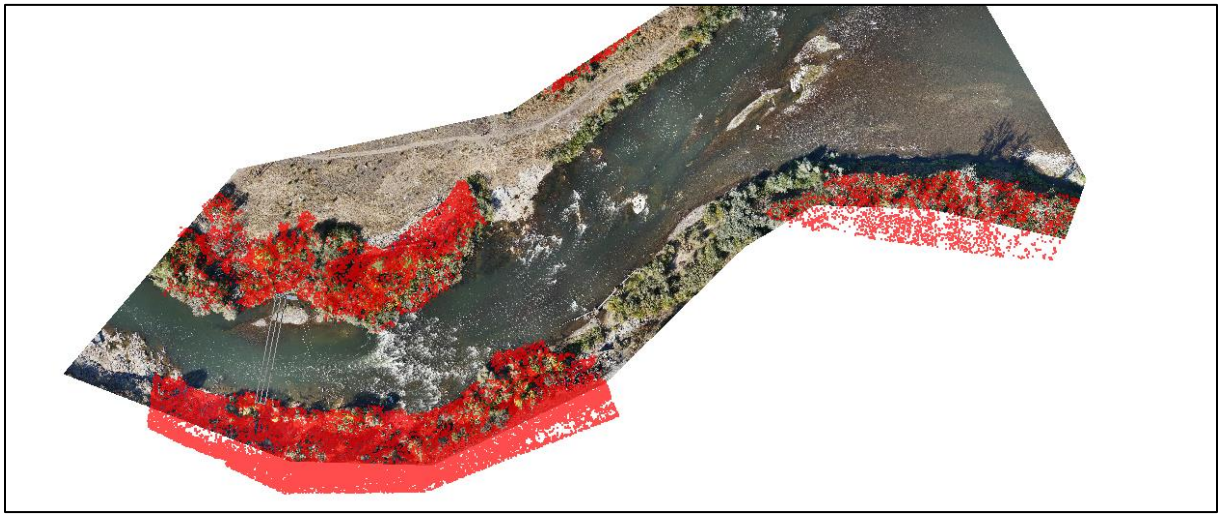

Figure 17. Lidar points utilized in gridding algorithm, overlaid onto 2016 Gold Ray Dam site imagery post dam removal.

With the exception of the dam, powerhouse, fish ladder, and other adjoining attributes, a large portion of the topography downstream of the dam remained unchanged due to most of the topography being made up of exposed bedrock, or large boulders. In large areas of dense vegetation, lidar proved beneficial in the retrieval of ground elevation points.

2.2.5 Accuracy Assessment

Uncertainty estimates for each input dataset are needed for the custom IDW algorithm developed in this work. Although there are numerous methods by which uncertainties could be obtained, in this study they were computed through an empirical accuracy assessment (i.e., a comparison of each "test" dataset against a "reference" or "control" dataset of higher accuracy). Between the RTK GNSS, lidar, sonar and SfM datasets, it is reasonable to assume that the RTK GNSS is the most accurate (i.e., has the lowest uncertainty). With this starting assumption, the RTK GNSS dataset was used as the reference dataset, while the lidar, sonar, and SfM datasets were used as test datasets. The accuracy assessment was performed in QCoherent LP360 software (ArcGIS extension version) Control Points function. Within this tool, a surface was generated from each test data set using a traditional Inverse Distance Weighting (IDW) algorithm with the search radius set to 1 meter and the power parameter set to 2. Vertical differences, dZ, were then calculated from each RTK GNSS point to each test surface in areas of overlap. The means and standard deviations of the dZ's were calculated (Table 9).

Table 9. Results of empirical accuracy assessment performed in LP360.

Dataset	μ **(m)**	σ **(m)**	**n**
Lidar	0.00	0.16	48
Sonar	0.02	0.09	26
SfM	-0.01	0.14	238

By convention, a positive bias, μ, signifies the control data set is higher than the surface generated from the test data set. Points lying outside the 3σ threshold were considered outliers, and were removed from the dataset. Since a bias was present for the sonar and SfM data sets, a vertical translation was performed to remove this bias prior to input into the gridding algorithm.

The σ values listed in Table 9 for the lidar, sonar, and SfM datasets were used as the input uncertainties in the custom IDW algorithm used to combine the data. For the RTK GNSS dataset, 0.05 m was used as the input uncertainty value, based on the 3DCQ of 0.05 m enforced within the Lieca data acquisition

software. This uncertainty value was chosen, based on the assumption that the vertical accuracy of RTK GNSS is equal to, or better than, the 3DCQ threshold.

The uncertainty estimates obtained in through this procedure are plausible indicators of the relative uncertainties for input into the custom IDW algorithm. However, these results should not be construed as an indication of the best achievable accuracy with any of the technologies listed. Factors contributing to the results listed in Table 9 include temporal changes between acquisition dates, surveying rugged terrain (Fig. 18), and utilizing some sparse data located in low vegetation areas (Fig. 19) in order to fill data voids in areas difficult to access by foot. Large areas of woody debris build-up (Fig. 20) were present throughout the AOI, which also contributed to larger vertical uncertainties.

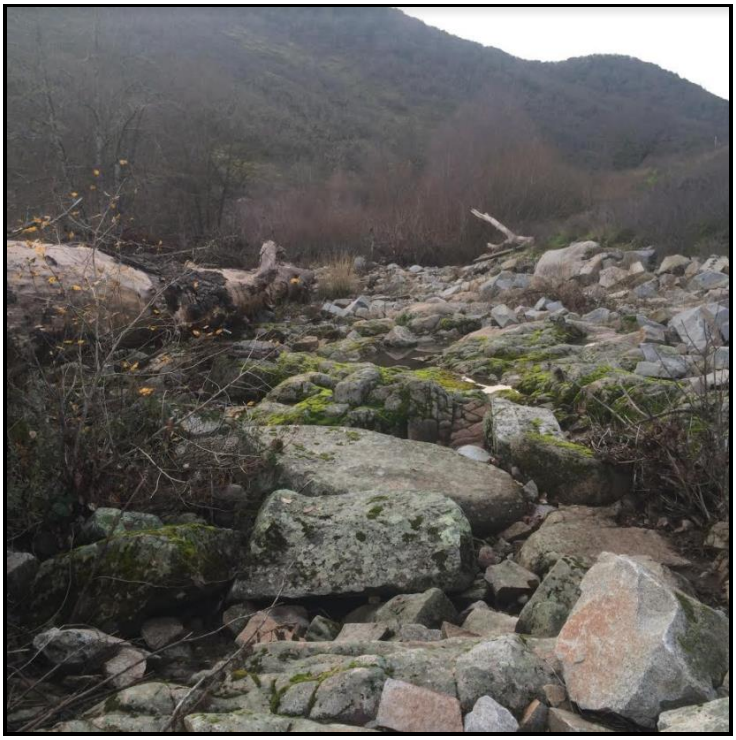

Figure 18. Rugged terrain within AOI

Figure 19. Low vegetation area difficult to access by foot (e.g. top of bank)

Figure 20. Areas of woody debris build up

2.2.6 IDW (Traditional)

The types of remote sensing technologies involved in this paper include: lidar, sonar, RTK GNSS, and SfM. All of these technologies produce datasets composed of irregularly-spaced (*X*,*Y*,*Z*) spatial coordinates, or point clouds. Due to the nature of point clouds' incomplete measurement of topographic and bathymetric features, interpolation of the sparse point cloud data is necessary to generate a surface needed for two- and three-dimensional hydrodynamic models, which, in turn, are required for whitewater park design.

To generate a regularly-spaced grid from the irregularly-spaced lidar, sonar, and RTK GNSS point clouds, an interpolation algorithm is used. One of the most widely-used interpolation algorithms is the inverse distance weighted (IDW) algorithm. This method is widely used by geoscientists, in part due to the ability to easily explain the IDW methodology summarized by the implementation of spatial auto-correlation (Kalkhan 2011). IDW is a type of deterministic interpolation method that uses a mathematical function to predict unknown values, where the predicted values are directly based on the surrounding measured values, weighted according to their distances from the interpolated point. Traditionally, the parameter setting for IDW is a power function, where the power variable, *p*, determines how rapidly weights fall off with distance from the interpolated point (Lu and Wong 2008):

$$\overline{z}_{IDW} = \frac{\sum_{i=1}^{n} z_i d_i^{-p}}{\sum_{i=1}^{n} d_i^{-p}} \tag{3}$$

where $\overline{z}_{IDW}$ is the interpolated value, and d_i is the distance from the grid node to the sample (measured) point *i* whose measured value is z_i. A common default value for the power parameter, *p*, is 2.
IDW is an appropriate interpolation method when interpolating from spatially correlated point datasets that are non-directionally dependent, are non-clustered and contain no data outliers (Rodriguez 2015). For elevation surfaces, the output from IDW results in flattening peaks and valleys unless the area of interest has a high point density.

2.2.7 IDW Uncertainty Weighted Gridding Algorithm

This paper implements a custom IDW algorithm that interpolates multi-sensor sparse point datasets, based not only on the traditional power parameter used to weight distances from a corresponding grid node, but also factors in a weight for the uncertainty of each dataset. The importance of this modified form of the IDW algorithm for this research (and, for that matter, for multi-sensor river mapping in general) is that

the integration of data sets from disparate surveying technologies requires a means of accounting for differing uncertainties of the inputs, as well as distance from the node.

$$\overline{z}_{UIDW} = \frac{\sum_{i=1}^{n} z_i d_i^{-p} u^{-q}}{\sum_{i=1}^{n} d_i^{-p} u^{-q}} \quad (4)$$

where u is the standard uncertainty (1 σ) of the data point z_i, q is the power parameter for uncertainty weighting, and all other variables are as defined previously. The algorithm was designed so that any number of datasets could be seamlessly gridded. The inputs for the algorithm are the multi-sensor datasets each in a ".las" file type (ASPRS 2013), the corresponding dataset uncertainties, the final grid resolution, search radius, and power variable used for the distance weighting. The algorithm first extracts all of the *X*, *Y*, and *Z* sparse data points from each ".las" file. It then calculates the gridding boundaries or extents, specifying x and y grid dimensions large enough to encompass all datasets. Next, grid node locations are calculated based on the grid resolution size input. Weights for each dataset are then calculated as the inverse square of the standard uncertainty (i.e., $q = 2$). At this point, the algorithm starts at the first grid node and calculates a distance to each sparse data point for all datasets. The input search radius is then used as a filter to only select data points within the search radius of the grid node. The final local mean value for the corresponding grid node is calculated using Eq. 4. This value is then stored, and the algorithm moves to the next grid node, and repeats this process for all grid nodes. The algorithm continues on to plot the gridded data, and save the result as an elevation heat map colored georeferenced DEM. The complete MATLAB Script is shown in the appendix.

3 Analysis

The customized IDW produced a seamless topographic-bathymetric DEM (Fig. 21) from four different multi-sensor datasets which can be used for a variety of hydrodynamic modeling functions. The gridded product appears to be a reasonable solution without significant artifacts. Since an independent, higher-accuracy "ground truth" data does not exist, an independent assessment for output accuracy cannot be performed, and without that data, validation of the solution is not possible. However, certain measures were taken during data acquisition to minimize data gaps, and maximize data overlap, since the higher the degree of overlap, the higher the probability of achieving a smooth, seamless and realistic integrated solution. This was performed by collecting bathymetry data during high water levels and topographic data during low water levels. Conforming to these conditions will produce the best possible dataset to perform the integration (Quadros et al. 2008).

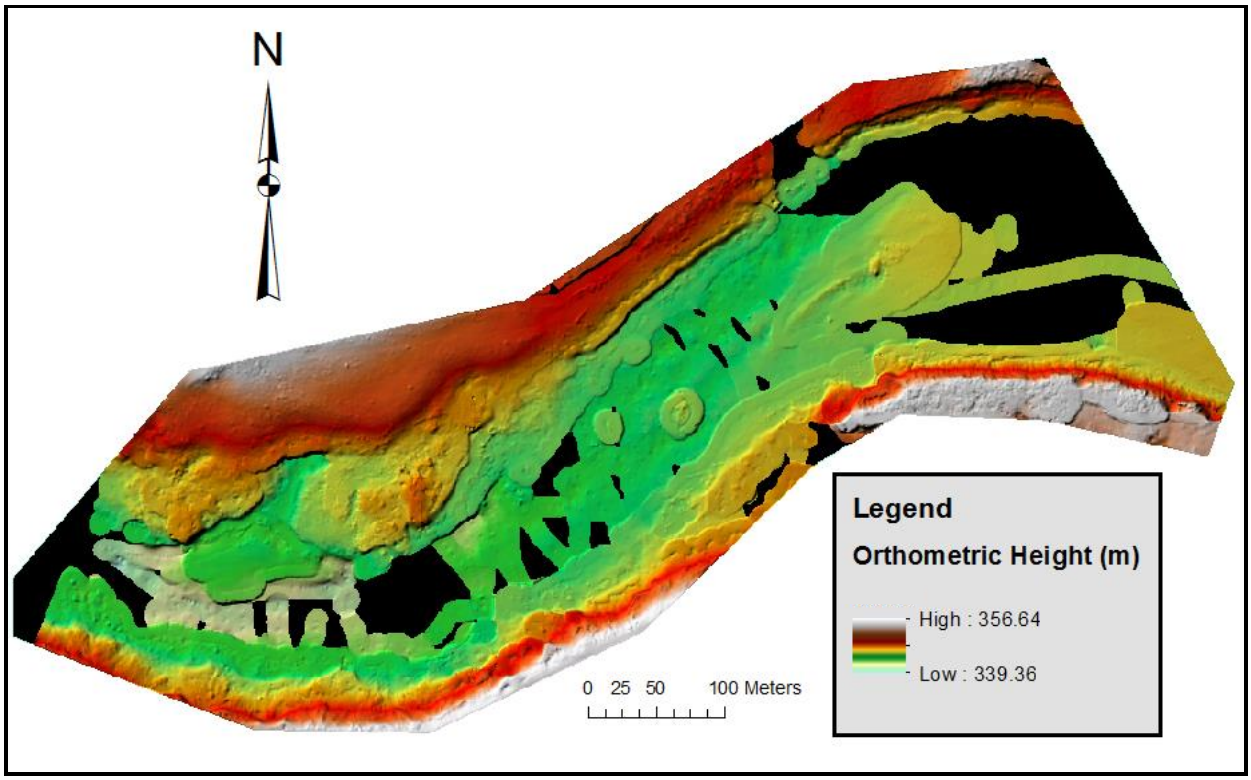

Figure 21. Final merged topobathymetric DEM for the AOI, shown as a hillshade in ArcGIS.

Before becoming an input in the gridding algorithm, the largest offsets within the datasets were ~0.15 m, which is reasonable for most hydrodynamic modeling functions. UAS-based SfM point data covered the dry river channel, and also collected data for limited portions of the submerged river channel. Since the refraction of light at the water surface is not taken into account in the creation of the SfM point cloud, the positional accuracy of the submerged data points is unknown; however, all submerged SfM points kept for modelling input aligned with either the echosounder data or RTK GNSS data within ± 0.15 m. As shown in Fig. 21, some data voids could not be interpolated across for a 0.5 m grid resolution due to the sparse nature of the echosounder data.

Overall, the algorithm processed over 40 million data points, the majority being densely populated SfM data points, and was able to generate a gridded DEM product in 36 hours which we consider reasonable, due to the complexity of merging disparate topobathymetric river data sets. The model allows for prominent river features to be detected, due to the high spatial resolution of the DEM (0.5 m), which could be a valuable tool for a white water park designer.

4 Discussion

River systems are inherently dynamic and experience geomorphic changes on a daily basis. Because of this, there are inherent temporal differences between the topographic and bathymetric surveys. In areas of bedrock there were no perceptible changes within the data collection timeframe. However, in areas of gravel and fine sediment, perceptible changes could be seen within the overlapping datasets. Overall, no drastic changes were present between the first and second survey and the previously acquired lidar data that was used. Figures 22 and 23 show an example cross section through all four datasets, displaying the agreement and accuracy of data overlap.

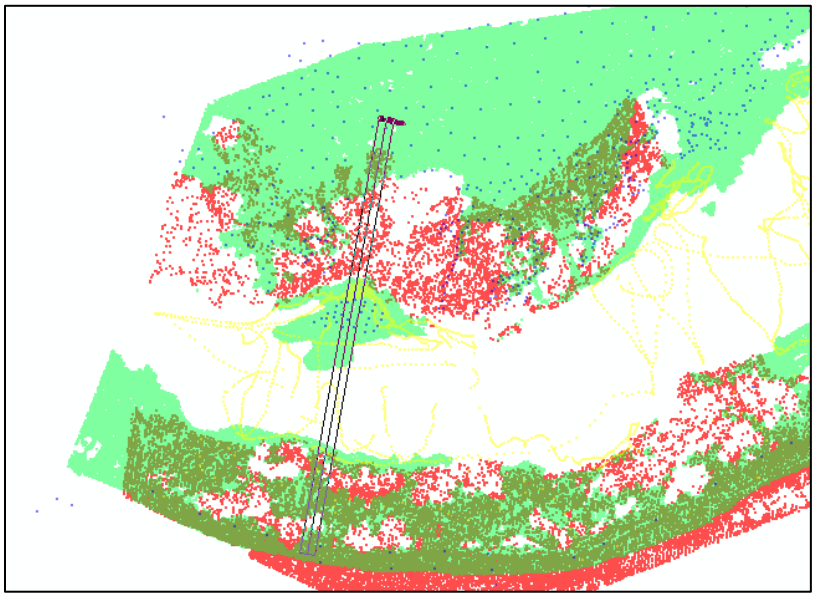

Figure 22. Overlapping data colored by data source (green-SfM, red-lidar, blue-RTK topo, yellow-sonar).

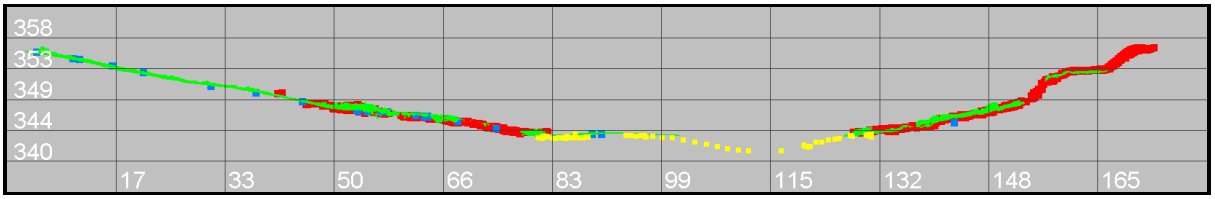

Figure 23. Cross section of merged data sets colored by classification (green-SfM, red-lidar, blue-RTK topo, yellow-sonar) with axes in meters.

An interesting phenomena discovered in the dataset was a 0.15-m systematic vertical offset between the SfM point data and the RTK GNSS data on areas of exposed bedrock. These areas of decreased accuracy were consistent throughout the AOI, occurring at locations far away from ground control targets, as expected, but also locations relatively close to ground control point targets. Figures 24 and 25 below

highlight the two locations where the phenomena occurred. In Fig. 24, it is interesting to see the profile view (bottom) of the data, where the SfM and RTK GNSS data agree within a couple of centimeters over the gravel and grassy portion of the island, but then jump up 0.15 m above the areas of exposed bedrock, only 10 m away. Fig. 25 shows a bedrock island where another 0.15 m vertical offset was seen between the RTK GNSS data and the SfM point data. However, this location was in the middle of the river, with the closest GCP being 26 m away.

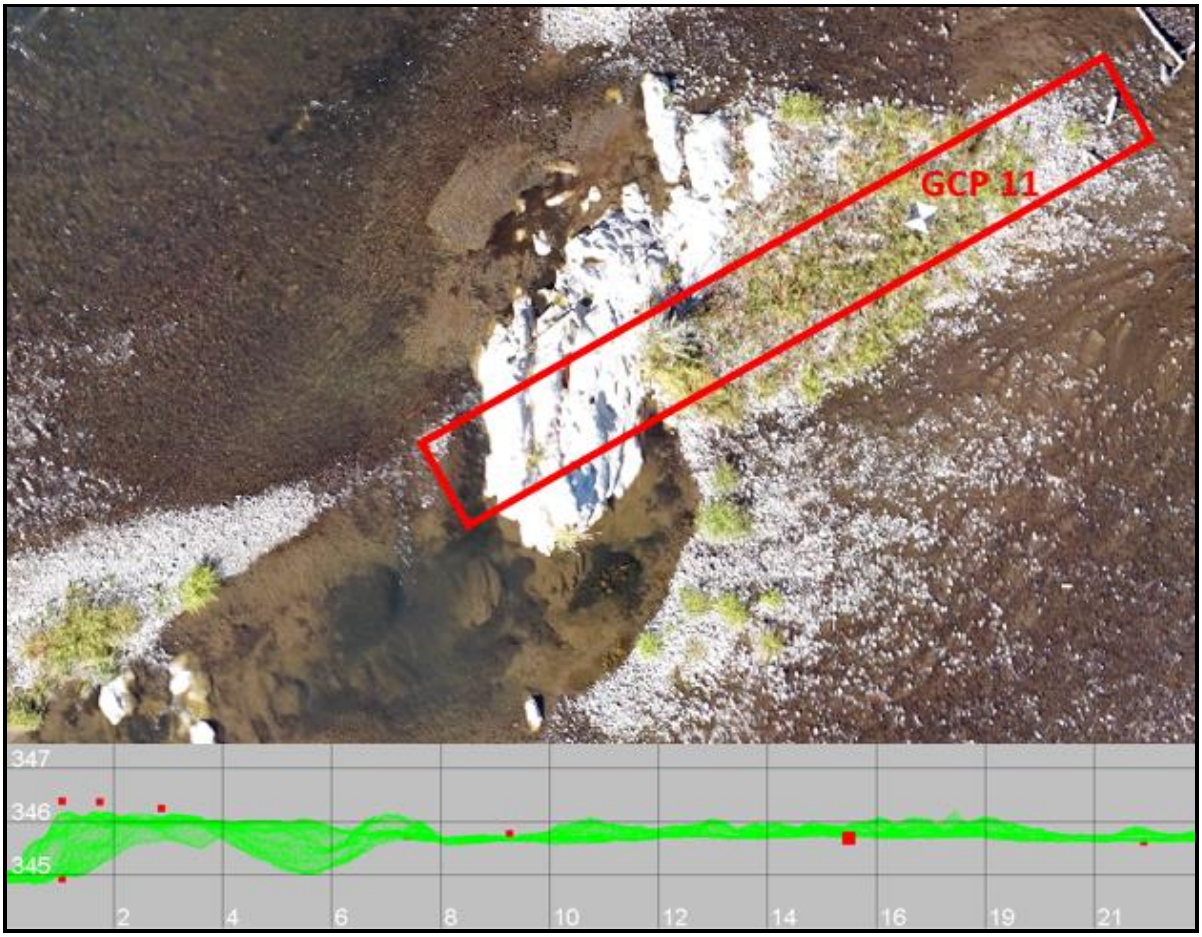

Figure 24: 15-cm vertical offset on exposed bedrock consistent throughout AOI (lower image). RTK GNSS (red dots) and SfM (green dots) shown in the bottom image. GCP 11 is represented as the largest red square.

Figure 25: Bedrock island with GCP10 located 26m away from island (closest GCP).

By analyzing the overlapping sparse data, the largest areas of uncertainty were in the submerged SfM datapoints, and the areas of exposed bedrock. In either case, these locations agreed within ± 0.16 cm of the RTK GNSS data, and with the use of the customized IDW algorithm performing a moving average on the combined dataset in order to grid the data, it is assumed that the final output DEM's accuracy should be close to, if not better than ± 0.16 m vertically.

5 Conclusions

Seamless, accurate, up-to-date topobathymetric DEMs are vital for river engineering and science applications, yet are notoriously difficult to generate. Challenges in river topobathymetric mapping range from logistical/environmental issues (variable and sometimes swift flows, changing channel characteristics) to technological and methodological (differing horizontal and vertical datums and spatial accuracies and resolutions of source data). This study takes a first step towards addressing these challenges by investigating a new, multi-sensor, multi-temporal fusion methodology for topobathymetric river mapping. The methods were tested by considering, as an example application, the evaluation of a proposed whitewater park site on the Rogue River in Oregon, near the site of the former Gold Ray Dam. Data collected for the project site included UAS imagery (processed in commercial SfM software to generate point clouds and orthoimagery), RTK GNSS transects and spot elevations, and single beam echosounder data. To facilitate a seamless merged product, the UAS and RTK GNSS data were collected under low discharge conditions (44 cms), while the sonar data were collected under high discharge

conditions (113-142 cms) after a period of heavy rain. The data were combined using a modified version of the IDW algorithm, which was custom developed for this study, and accounts for both distance and the differing uncertainties of the inputs.

The methods appear quite promising for seamless topobathymetric river mapping. The UAS, RTK, and single beam echosounder data acquisitions were conducted safely and efficiently over a span of ~3 months (approximately 3 days of data acquisition, total). The acquisition strategy that involved using land-based survey technologies at low-flow river stages and boat-based methods at high-flow stages was determined to enable highly-beneficial overlap for merging the data. The custom IDW algorithm was found to work well for the data merge portion of the project, providing a high-resolution (0.5 m), seamless, and relatively gap-free topobathymetric DEM. Implemented in MATLAB, the custom IDW algorithm was reasonably computationally efficient, although optimization of the code is a recommended area of further research. Conceptually, the modified IDW algorithm developed and tested in this work is superior to the conventional IDW algorithm in its ability to handle greatly differing uncertainties in the input source data from disparate surveying technologies. In this study, quantitative evaluation of the final topobathymetric DEM was limited, however, due to a lack of additional ground truth for performing accuracy assessments. Visual assessment of the output confirmed that the DEM was free of seamlines and other noticeable artifacts. A recommendation for future work is to collect additional reference data for the site to both quantify the accuracy of the merged topobathymetric product and refine the parameters in the custom IDW algorithm – particularly, the relative weighting between distance from the interpolated point and uncertainty.

Another recommendation for future work is to collect additional bathymetric data, in order to minimize data voids in the subaqueous portion of the AOI. One way to do this would be to collect more in-stream hand-held RTK GNSS rod occupations when the river is at the lowest level. Data collection using the echosounder at high river flows was unsuccessful in whitewater areas, whereas, these same areas could potentially be accessed on foot at lower river levels. If available, a multibeam echosounder (MBES) or phase differencing bathymetric sonar (PDBS) would be highly beneficial. Small, autonomous survey boats are also of interest for river mapping, and could be incorporated into follow-on research. Additionally, topobathymetric lidar would be another source data to investigate merging using the methods of this study. Finally, a follow-on study investigating the degradation of the SfM-derived point clouds, due to the areas of highly-reflective bedrock, is recommended.

References

Alho, P., Hyyppä, H., and Hyyppä, J. (2009). "Consequence of DTM precision for flood hazard mapping: A case study in SW Finland." *Nordic Journal of Surveying and real Estate Research*, 6, 21–39.

American Whitewater. (2007). "Whitewater parks – Considerations and case studies." <https://www.americanwhitewater.org/> (Jan. 18, 2017).

Anderson, J. (2016). "Technical Memorandum No. 1: Description of Project." *McLaughlin Whitewater Design Group*, 1-7.

ASPRS. (2013). "LAS SPECIFICATION VERSION 1.4-R13." *The American Society for Photogrammetry & Remote Sensing*, 1–28.

Binns, N. (1994). "Long-term responses of trout and macrohabitats to habitat management in a Wyoming headwater stream. *North American Journal of Fisheries Management* 14(1): 87–98.

Buttner, O. (2007). "The influence of topographic and mesh resolution in 2D hydro- dynamic modelling for floodplains and urban areas." *European Geosciences Union. Geophysical Research Abstracts*, 9(08232).

Davidson, M.A. and Miglarese, A.H. (2003). "Digital Coast". *Photogrammetric Engineering & Remote Sensing*, *69*(10), pp.1127-1131.

Ferreira, H., Almeida, C., Martins, A., Almeida, J., Dias, N., Dias, A., and Silva, E. (2009). "Autonomous Bathymetry for Risk Assessment with ROAZ Robotic Surface Vehicle." 1–6.

Flener, C., Vaaja, M., Jaakkola, A., Krooks, A., Kaartinen, H., Kukko, A., Kasvi, E., Hyyppä, H., Hyyppä, J., and Alho, P. (2013). "Seamless mapping of river channels at high resolution using mobile liDAR and UAV-photography." *Remote Sensing*, 5(12), 6382–6407.

Hardy, R.J., Bates, P.D., and Anderson, M.G. (1999). "The importance of spatial resolution in Hydraulic models for floodplain environments." *Journal of Hydrology* 216 (1–2), 124–136.

Harig, A, Fausch, K, and Young, M. (2000). "Factors influencing success of greenback cutthroat trout translocations". *North American Journal of Fisheries Management* 20: 994–1004.

HDR. (2009). "Jackson County Gold Ray Sediment Assessment Report." 1-173.

Horritt, M.S., Bates, P.D., and Mattinson, M.J. (2006). "Effects of mesh resolution and topographic representation in 2D finite volume models of shallow water fluvial flow." *Journal of Hydrology* 329 (1–2), 306–314.

Javernick, L., Brasington, J., and Caruso, B. (2014). "Modeling the topography of shallow braided rivers using Structure-from-Motion photogrammetry." *Geomorphology*, Elsevier B.V., 213, 166–182.

Kalkhan, M. A. (2011). *Spatial Statistics: Geospatial Information Modeling and Thematic Mapping*. Boca Raton, Florida: CRC Press.

Koljonen, S., Huusko, A., Mäki-Petäys, A., Louhi, P., and Muotka, T. (2012). "Assessing habitat suitability for juvenile atlantic salmon in relation to in-stream restoration and discharge variability." *Restoration Ecology*, 21, 344–352.

Larscheid, J., and Hubert, W. (1992). "Factors influencing the size structure of brook trout and brown trout in southeastern Wyoming mountain streams." *North American Journal of Fisheries Management* 12(1): 109–117.

Lejot, J., Delacourt, C., Piégay, H., Fournier, T., Trémélo, M.L. and Allemand, P. (2007). "Very high spatial resolution imagery for channel bathymetry and topography from an unmanned mapping controlled platform." *Earth Surface Processes and Landforms*, 32(11), pp.1705-1725.

Loomis, J. (2011). "Fort Collins Whitewater Park Economic Assessment." 1–13.

Lu, G. Y., and Wong, D. W. (2008). "An adaptive inverse-distance weighting spatial interpolation technique." *Computers and Geoscience* 34: 1044-1055

Maxwell, S.L., and Smith, A.V. (2007). "Generating river bottom profiles with a Dual-Frequency Identification Sonar (DIDSON)." *North American Journal of Fisheries Management*, 27, 1294–1309.

Merwade, V., Cook, A., and Coonrod, J. (2008). "GIS techniques for creating river terrain models for hydrodynamic modeling and flood inundation mapping." *Environmental Modelling and Software*, 23(10–11), 1300–1311.

Moorman, M. K., Schlatter, B. E., and Hurd, A. R. (2007). "Adventure Recreation." *Journal of Physical Education, Recreation & Dance*, 78(9), 22–26.

Quadros, N., Collier, P., and Fraser, C. (2008). "Integration of bathymetric and topographic Lidar: a preliminary investigation." *The International Archives of the Photogrammetry Remote Sensing and Spatial Information Sciences Beijing 2008*, XXXVII(B8), 1299–1304.

Raber, G.T., Jensen, J.R., Hodgson, M.E., Tullis, J.A., Davis, B.A., and Berglund, J. (2007). "Impact of LIDAR nominal post-spacing on DEM accuracy and flood zone delineation." *Photogrammetric Engineering and Remote Sensing*, 73(7), 793–804.

Rodriguez, R. R. (2015). "Integration of Topographic and Bathymetric Digital Elevation Model using ArcGIS Interpolation Methods: A Case Study of the Klamath River Estuary." 1-119.

Roni, P., Hanson, K., Beechie, T. (2008). "Global review of the physical and biological effectiveness of stream habitat rehabilitation techniques." *North American Journal of Fisheries Management* 28(3): 856–890.

Slocum, R.K., and Parrish, C.E. (2017). "Simulated Imagery Rendering Workflow for UAS-Based Photogrammetric 3D Reconstruction Accuracy Assessments." *Remote Sensing*, 9(4), 396.

Watershed Sciences. (2009). “Lidar Remote Sensing Data Collection – Department of Geology and Mineral Industries – Medford.” 1-21.

APPENDIX

Kellum MATLAB Algorithm:

runKellumIDW.m

```
%% Run Kellum IDW with '.las'inputs
% Depedencies: lasdata.m (Author: Teemu Kumpumki / Tampere University of
% Technology 2014) available here:
% https://www.mathworks.com/matlabcentral/fileexchange/48073-lasdata

clc
clear
close all

FILENAMES = {'C:\Research_Kory\RogueRiver\Edited_Las_files\RTK_topo_edited_groundpts02.las',...
             'C:\Research_Kory\Rogue River\Edited_Las_files\Sonar_edited_bathypts02_Translated.las',...
              'C:\Research_Kory\Rogue River\Edited_Las_files\SfM_Edited_groundpts02_translated.las',...
              'C:\Research_Kory\Rogue River\Edited_Las_files\Lidar_All_Edited_groundpts02.las'};


ACCURACY{1} = 0.05;  %3 sigma standard deviation of the mean per dataset
ACCURACY{2} = 0.09;
ACCURACY{3} = 0.14;
ACCURACY{4} = 0.16;

DX = 0.5; %0.5 meter resolution
RADIUS = 5;
POWER = 2;

%% Processing Code
ndatasets = numel(FILENAMES);
x=cell(ndatasets,1);
y=cell(ndatasets,1);
z=cell(ndatasets,1);
fprintf('Loading Point Data... %s\n',datestr(now));
for iFilenumIndex = 1:ndatasets
   [dname,fname,ext] = fileparts(FILENAMES{iFilenumIndex});
   fprintf('\t Loading (%.f/%.0f) [%s]: %s\n',iFilenumIndex,ndatasets,datestr(now),[dname '/' fname ext]);
   [x{iFilenumIndex},y{iFilenumIndex},z{iFilenumIndex}] = readxyz(FILENAMES{iFilenumIndex});
end
fprintf('Finished Loading Data... %s\n',datestr(now));
[xi,yi]=calcGridBounds(x,y,DX);
[zg,npts]=KellumIDW(x,y,z,ACCURACY,xi,yi,RADIUS,POWER);

%% Plot Data
figure(1)
pcolor(xi,yi,zg);shading flat
figure(gcf)
```

```
title('IDW gridded data');
axis equal

%% Write Geotiff
Zdata=zg;
R = maprasterref('RasterSize',[numel(yi) numel(xi)],'ColumnsStartFrom','South');
R.XWorldLimits = [xi(1) xi(end)];
R.YWorldLimits = [yi(1) yi(end)];
key.GTModelTypeGeoKey = 1;
key.GTRasterTypeGeoKey = 1;
key.ProjectedCSTypeGeoKey = 32767;
geotiffwrite('C:\Research_Kory\Matlab\zdata_geotiff.tif',Zdata,R,'GeoKeyDirectoryTag',key)
geoZ  = imread('zdata_geotiff.tif');
fprintf('Class type of Z: %s\n', class(Zdata))
fprintf('Class type of data in GeoTIFF file: %s\n', class(geoZ))
fprintf('Does data in GeoTIFF file equal Z: %d\n', isequal(geoZ, Zdata))
figure
mapshow('zdata_geotiff.tif','DisplayType','texturemap')
title('Peaks - Stored in GeoTIFF File')
```

readxyz.m

```
function [x,y,z]=readxyz(filename)

[~,~,ext] = fileparts(filename);

tf=strcmp(ext,'.las');

if tf==1
   [x,y,z] = readLasToXYZ(filename);
else
   [x,y,z] = readCsvToXYZ(filename);
end

end
```

readLasToXYZ.m

```
function [x,y,z] = readLasToXYZ(filename)

dataStruct = lasdata(filename);
x = dataStruct.x;
y = dataStruct.y;
z = dataStruct.z;

end
```

readCsvToXYZ.m

```
function [x,y,z] = readCsvToXYZ (filename)

dat = importdata(filename);

if isstruct(dat)
   x = dat.data(:,1);
   y = dat.data(:,2);
   z = dat.data(:,3);
else
   x = dat(:,1);
   y = dat(:,2);
   z = dat(:,3);
end

end
```

calcGridBounds.m

```
%This function will develop a grid x and y
function [xi,yi]=calcGridBounds (x,y,dx)

ndatasets = numel(x);

MinX = nan(ndatasets,1);
MaxX = nan(ndatasets,1);
MinY = nan(ndatasets,1);
MaxY = nan(ndatasets,1);

for countIndex= 1:ndatasets
   MinX(countIndex)=min(x{countIndex}(:));
   MinY(countIndex)=min(y{countIndex}(:));
   MaxX(countIndex)=max(x{countIndex}(:));
   MaxY(countIndex)=max(y{countIndex}(:));
end

MinXfinal = min(MinX);
MinYfinal = min(MinY);
MaxXfinal = max(MaxX);
MaxYfinal = max(MaxY);

xi = MinXfinal:dx:MaxXfinal;
yi = MinYfinal:dx:MaxYfinal;

end
```

KellumIDW.m

```
function [zg,npts]=KoryKellumIDW(x,y,z,accuracy,xi,yi,r,p)

%%xi grid array 1x n (n=#elements)
%%yi grid array

%% Make Sparse Data all Column Arrays
x = x(:);
y = y(:);
z = z(:);

%% Loop through variables

zg = nan(numel(yi),numel(xi)); % preallocate variable
npts = nan(numel(xi),numel(yi)); %preallocate
%%
startTime = now; %Loop Time Code
for iGridXindex=1:numel(xi) %Grid Indexing
   for jGridYindex=1:numel(yi)

      loopXval = xi(iGridXindex); %real node coordinates
      loopYval = yi(jGridYindex);

     %%Calculate Accuracy weights from all data sets
     Wacc = calculateWacc(accuracy);

      for kDatasetIndex = 1:numel(x)%loop through datasets
         dataSetXpts = x{kDatasetIndex};
         dataSetYpts = y{kDatasetIndex};
         D = calcDist2Points(loopXval,loopYval,dataSetXpts,dataSetYpts);%nodeX,nodeY,x,y
         inRadiusIndex = find(D<=r);
         Zvals{kDatasetIndex}=z{kDatasetIndex}(inRadiusIndex);%find z values within Distance range
and stores in cell
         wAccuracy{kDatasetIndex}=ones(numel(Zvals{kDatasetIndex}),1)*Wacc{kDatasetIndex};
         Dvals = D(inRadiusIndex);%Finds distances correlated to matching z values within radius
         wDist{kDatasetIndex} = 1./(Dvals.^p);  %calcs weight for each z val and stores in cell

      end
      %at this point all Z values within search radius and corresponding
      %wDist and wAcc are calculated and stored in cell array

      %final gridded zvalue weighted by distance and accuracy
      for lDatasetIndex = 1:numel(x)

Zn{lDatasetIndex}=sum(Zvals{lDatasetIndex}.*wDist{lDatasetIndex}.*wAccuracy{lDatasetIndex});
%numerator of zfinal
```

```
        Zd{lDatasetIndex}=sum(wDist{lDatasetIndex}.*wAccuracy{lDatasetIndex});%denomenator of
zfinal

    end

    numerator=0;
    for lDatasetIndex=1:numel(x)
       iNum=Zn{lDatasetIndex};
       numerator=numerator+iNum;
    end

    denomenator=0;
    for lDatasetIndex=1:numel(x)
       jDen=Zd{lDatasetIndex};
       denomenator=denomenator+jDen;
    end

    Zfinal=numerator./denomenator;

    zg(jGridYindex,iGridXindex)=Zfinal; %places value in allocated matrix

    npts(jGridYindex,iGridXindex)=numel(Dvals);
  end

  loopStatus(startTime,iGridXindex,numel(xi),1);
end


end
```

loopStatus.m

```
function loopStatus(startTime,curLoopNum,nLoops,nskip)
% LOOPSTATUS outputs status of for loop to the command line
%   Outputs the current loop number, the current time, and the expected
%   time the loop will finish to the Matlab command line.  This is useful
%   when running long for loops, to estimate how far along they are.
%
%   Simply add a 'startTime = now'; command before the loop, and then add
%   this function at the end of the loop.
%
%   Note: The estimate relies on the for loop remaining relatively constant
%   throughout the duration of the collect.
%
% Inputs:
%   - startTime  : 1 : datenum : matlab datenum of time when the loop began
%   - curLoopNum : 1 : int     : the current loop number
%   - nLoops     : 1 : int     : the total number of loops
```

```
%   - nskip      : 1 : int     : the total status lines to skip
%
% Outputs:
%   - n/a
%
% Examples:
%   NLOOPS = 1000;
%   NSKIPS = 10;
%   startTime = now;
%   for i=1:NLOOPS
%       pause(.05)
%       loopStatus(startTime,i,NLOOPS,NSKIPS)
%   end
%   datestr(now)
%
% Dependencies:
%   - n/a
%
% Toolboxes Required:
%   - n/a
%
% TODO:
%
% Author       : Richie Slocum
% Email        : slocumr@oregonstate.edu
% Date Created  : 14-Apr-2016
% Date Modified : 14-Apr-2016

if nargin==3
   nskip = 1; %default to output every loop
end

if mod(curLoopNum,nskip)==0
   t = now - startTime; %time it took for the first nLoops
   avgLoopTime = t/(curLoopNum);
   loopsRemaining = nLoops-curLoopNum;

   estimTime = avgLoopTime*loopsRemaining;

   estimDatenum = datestr(now + estimTime);

   fprintf('%.0f/%.0f \t Now: %s \t Expected: %s \t Remaining: %s\n',...
      curLoopNum,nLoops,datestr(now),estimDatenum, ...
      datestr(estimTime,'dd:HH:MM:SS'));
end

end
```

calculateWacc

```
%Calculates a weight for corresponding dataset uncertainty
function Wacc = calculateWacc(accuracy)

Wdenominator=0;
 for iAccIndex = 1:numel(accuracy) %loops through accuracy matrix
    iDenom = 1./accuracy{iAccIndex}^2; %last part of equation denominator
     Wdenominator = Wdenominator + iDenom;
  end

 for jAccIndex = 1:numel(accuracy)
    iAcc = 1./accuracy{jAccIndex}^2; %first part of equation denominator
    Wacc{jAccIndex} = iAcc*(1./Wdenominator);
 end

end
```

calcDist2Points.m

```
function D = calcDist2Points(nodeX,nodeY,xsparse,ysparse)
% calculate distance from node to sparse pts
D = sqrt((nodeY-ysparse).^2+(nodeX-xsparse).^2);
end
```

(THIS PAGE INTENTIONALLY LEFT BLANK)